Kinetically Controlled Autocatalytic Chemical Process for Bulk Production of Bimetallic Core—Shell Structured Nanoparticles

Fadlilatul Taufany,[†] Chun-Jern Pan,[†] John Rick,[†] Hung-Lung Chou,[†] Mon-Che Tsai,[†] Bing-Joe Hwang,*,[†,‡] Din-Goa Liu,[‡] Jyh-Fu Lee,[‡] Mau-Tsu Tang,[‡] Yao-Chang Lee,[‡] and Ching-Iue Chen[‡]

[†]Nanoelectrochemistry Laboratory, Department of Chemical Engineering, National Taiwan University of Science and Technology, Taipei 106, Taiwan, Republic of China, and [‡]National Synchrotron Radiation Research Center, Hsinchu 300, Taiwan, Republic of China

The bulk fabrication of advanced bimetallic nanostructures with exceptional catalytic,[1,2] magnetic,[3,4] thermal,[5] and optical[6,7] properties is a prerequisite for their wide applicability in nanotechnology. Bimetallic core—shell nanostructures, made with an active-metal shell supported on another metal as a core element, are emerging as one of the most promising solutions able to address these requirements. Such bimetallic core—shell nanostructures with enhanced nanoscale properties are of interest due to their potential as highly efficient catalysts,[8,9] magnetic components for ultra-high-density memory devices,[8,9] and sensors in the biomedical field.[10] Among bimetallic core—shell nanostructures, Pt ultrathin layered shells on the surface of a dimensionally stable M metal core ($M_{core}Pt_{ultrathin-shell}$, where M is the noble and 3d-transition metals) nanoparticles (NPs) are achieving prominence due to their multifunctionalities and enhanced properties that can be broadly exploited for those applications.[11−13] The most widespread role of platinum is as a catalyst, particularly in the automobile industry, petrochemical industry, fuel cells, biosensors, etc.[14] As Pt is tremendously expensive, it is highly beneficial to reduce the amount of Pt. The $M_{core}Pt_{ultrathin-shell}$ NPs comprise a very low Pt content in their outer ultrathin layer shell and are one of the best solutions to addressing this issue, an approach that can cut back the Pt cost while enhancing catalytic activity.

Although these bimetallic core—shell nanostructures are of significance, the conventional synthetic approaches have not been successful in producing high-quality core—shell NPs. These difficulties are due to several factors including random nucleation

ABSTRACT
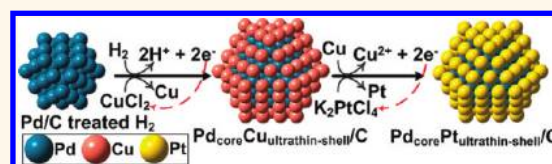
Although bimetallic core@shell structured nanoparticles (NPs) are achieving prominence due to their multifunctionalities and exceptional catalytic, magnetic, thermal, and optical properties, the rationale underlying their design remains unclear. Here we report a kinetically controlled autocatalytic chemical process, adaptable for use as a general protocol for the fabrication of bimetallic core@shell structured NPs, in which a sacrificial Cu ultrathin layer is autocatalytically deposited on a dimensionally stable noble-metal core under kinetically controlled conditions, which is then displaced to form an active ultrathin metal-layered shell by redox—transmetalation. Unlike thermodynamically controlled underpotential deposition processes, this general strategy allows for the scaling-up of production of high-quality core—shell structured NPs, without the need for any additional reducing agents and/or electrochemical treatments, some examples being Pd@Pt, Pt@Pd, Ir@Pt, and Ir@Pd. Having immediate and obvious commercial potential, Pd@Pt NPs have been systematically characterized by *in situ* X-ray absorption, electrochemical-FTIR, transmission electron microscopy, and electrochemical techniques, both during synthesis and subsequently during testing in one particularly important catalytic reaction, namely, the oxygen reduction reaction, which is pivotal in fuel cell operation. It was found that the bimetallic Pd@Pt NPs exhibited a significantly enhanced electrocatalytic activity, with respect to this reaction, in comparison with their monometallic counterparts.

KEYWORDS: kinetically controlled · autocatalytic · core—shell · Pd@Pt · Pt ultrathin layer

processes and inhomogeneous growth of the heterometallic component on core surface NPs.[15] Thus, it is necessary to develop and couple new NP synthesis methods with first-principles theoretical design, as it gives mechanistic insight into the atomistic surface chemistry governing the enhanced properties and provides the groundwork for NP fabrication.

Here we report a first-principles theoretical guided synthesis and characterization of selected core—shell NPs and demonstrate their unique properties using an oxygen reduction reaction (ORR), a key reaction for the practical implementation of hydrogen fuel cells. We additionally examine the general applicability of the designed strategy for the other core—shell NPs, e.g., Pt@Pd, Ir@Pt, and Ir@Pd. The $Pd_{core}Pt_{ultrathin-shell}$ NPs were chosen as a primary example since Adzic et al.[12] found that the ORR activity of a Pt-layered shell supported on Au(111), Rh(111), Pd(111), Ru(0001), and Ir(111) follows a volcano-type profile with respect to the center of their d-bands, with the Pt-layered shell on Pd(111) showing the highest activity, and thereby could address the principal drawbacks in this application, namely, the sluggish kinetics and high Pt-loading associated with the ORR.[16,17]

Similarly, the fabrication of these $Pd_{core}Pt_{ultrathin-shell}$ NPs is an ongoing challenge. In the established redox—transmetalation approach,[9] the Pd-core NPs are directly refluxed with the Pt-salt precursor, often leading to the formation a dense array of Pt dendritic branches, rather than a uniform Pt ultrathin layer shell.[18,19] This outcome has been attributed to the small lattice mismatch (~0.77%) between these two metals, as the spontaneous epitaxial growth of Pt on the Pd core is thermodynamically favored.[20,21] When these Pd NPs undergo a redox reaction with the Pt ions, which have a higher equilibrium potential, the unwanted dissolution of the Pd NPs also takes place. Toshima et al.[22,23] protected the surface of the Pd core with a sacrificial hydrogen layer before contacting with Pt ions. This redox approach, in which the adsorbed hydrogen layer was oxidized by Pt ions, prevents the dissolution of the Pd core. However, producing a Pt ultrathin layer remains a challenging task, since the previously formed Pt layer is still active toward hydrogen and so can create additional thick Pt layers.

Adzic et al.[12,13,24,25] used the redox displacement of previously deposited Cu, by the under-potential deposition (UPD) of adatoms on a Pd surface, to form Pt-monolayered NPs. UPD involves the deposition of an adatom on a foreign-metal substrate at a potential more positive than that predicted by the Nernst equation. Applying this potential makes the strength of the interactions between the adatom and the substrate greater than among the adatoms, during spontaneous deposition under thermodynamically controlled conditions. However, since the synthesis was carried out electrochemically on a glassy carbon electrode, the resulting quantity of Pt monolayered electrocatalyst was limited to a few tens of micrograms.[26]

To scale-up production, we started from first principles using DFT to search for a nonelectrochemical way of depositing a Cu ultrathin layer on a Pd/C core, which we could displace to form a Pt ultrathin layer shell. The present approach, which overcomes the Cu-UPD
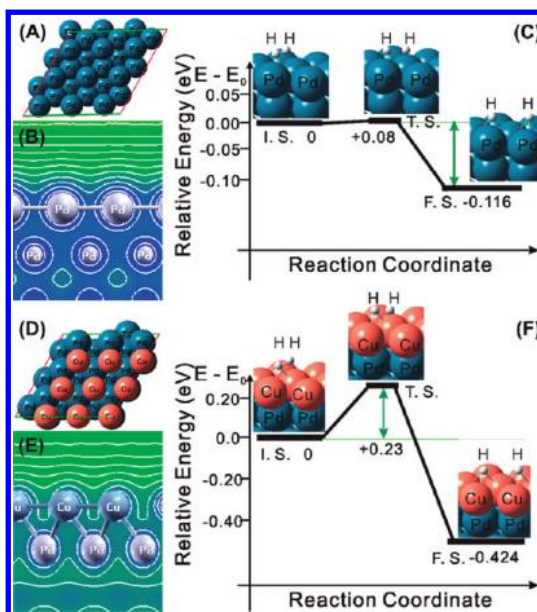

Figure 1. (A) DFT model of the top view of the Pd(111) slab system, together with (B) its corresponding contour maps and (C) potential energy profile for the dissociative adsorption of hydrogen, in comparison with that of the $Cu_{ultrathin-shell}Pd_{core}$(111) slab system (D–F).

process's limited production capacity, utilizes the strong reducing ability of the metal-hydride/adsorbed hydrogen on the palladium's surface.[27] Here the electrons from the sacrificial oxidation of the adsorbed hydrogen layer on Pd are used for the reduction of the Cu salt and the deposition of a Cu ultrathin layer on the Pd core's surface. It is well known that hydrogen is easily adsorbed and split on the surface of noble metals to form hydrides. This hydride/adsorbed hydrogen has a strong reducing ability, suggesting very low equilibrium potential.[22,23] When metal ions having a higher equilibrium potential (e.g., Cu^{2+}, $Cu^{2+} + 2e^{-} \rightarrow Cu$, 0.34 V) approach the adsorbed hydrogen, they can be reduced by sacrificial oxidation of the adsorbed hydrogen, resulting in the deposition of Cu on the Pd surface under favorable redox condition ($\Delta E° > 0$). Since the Cu metal surface is substantially inactive toward hydrogen, there is a large barrier against Cu dissociating the hydrogen molecule, e.g., adsorbing and splitting it to form hydride. The lack of hydride on the Cu surface prevents the initiation of self-nucleation, leading to the formation of a Cu ultrathin layer on the Pd surface ($Pd_{core}Cu_{ultrathin-shell}$ structure). Our DFT modeling study clearly predicts this sort of kinetically controlled behavior (Figure 1). The Cu ultrathin layer is sacrificially oxidized by Pt redox—transmetalation, to form a Pt ultrathin layer on Pd.

This autocatalytic process has several advantages: (1) no additional reducing agent and electrochemical treatments are needed, (2) layer deposition occurs only on the core's surface, (3) the original size and shape of the core are maintained, and (4) significant quantities of the core—shell NPs can be prepared.

RESULTS AND DISCUSSION

We have used DFT modeling to illustrate the relationship between the metal's surface with its adsorbate and various catalytic processes,[28−30] *e.g.*, to show the way hydrogen adsorbate dissociates on Pd(111) and $Cu_{ultrathin-shell}Pd_{core}$(111) surfaces. In Figure 1A, the Pd(111) system was modeled using four-layer slabs of a Pd fcc lattice, nine atoms per layer, a 3 × 3 supercell with dimensions of $8.253 \times 8.253 \times 18.493$ Å^3, exposing the (111) facet. A similar configuration was adopted for the $Cu_{ultrathin-shell}Pd_{core}$(111), with the top layer of Pd atoms being replaced with Cu atoms (Figure 1D). Its corresponding contour map, which depicts the electron density contour of the plane cut through the Cu atom and Pd atom at the center site (Figure 1E), is clearly different from that of Pd(111) (see Figure 1B). This, consequently, may give different energy barriers for hydrogen dissociation on these two metal surfaces.

The geometries of the adsorbed sites in each pathway and their corresponding potential energy profiles are illustrated in Figure 1. In the initial state (IS), the hydrogen molecule preferentially adsorbs on 3-fold sites of the Pd(111) and $Cu_{ultrathin-shell}Pd_{core}$(111) slab surfaces, since these sites have the larger coordination number and, thus, present the most stable sites. At the transition state (TS), the bond breaking of hydrogen molecules takes place given a sufficient energy. Simultaneous bond formation between the adsorbate and the substrate takes place in the final state (FS). We have calculated the dissociation energy barriers (E_d) involved in hydrogen bond breaking on both slab surfaces. The pure Pd(111) slab has a dissociation energy barrier of only 0.08 eV; thus the Pd surface easily adsorbs and spontaneously splits hydrogen.[31] The dissociation energy barrier (0.23 eV) on the $Cu_{monolayer}Pd_{core}$(111) surface is significantly higher, implying that the Cu-monolayer layer is inert toward hydrogen and therefore cannot form additional thick Cu layers because the process is kinetically controlled. This contrasts with conventional thermodynamically controlled Cu-UPD processes.

This Cu ultrathin layer then generates a Pt ultrathin layer on Pd by redox−transmetalation; that is, the Cu ultrathin layer is sacrificially oxidized to generate electrons for the reduction of Pt, thereby depositing a Pt ultrathin layer on the Pd core (see Figure 2A). To characterize the Pd−Cu and Pd−Pt core−shell structures, we performed *in situ* X-ray absorption (XAS) measurements,[32−39] as shown in Figure 2. XAS spectroscopy, encompassing both the X-ray absorption near-edge structure (XANES) and the extended X-ray absorption fine structure (EXAFS), is a powerful structural/characterization technique for investigating oxidation states and the environment surrounding an absorbing atom. The modules of the Pd k-edge of the Fourier transform (FT) obtained for all the $Pd_{core}Pt_{ultrathin-shell}$/C NP reaction steps during preparation are shown in Figure 2B. The corresponding EXAFS fitting parameters are listed in the Supporting Information, Table S1. In stage 1, compared to the Pd foil, the transformation of the commercial Pd/C NPs shows an additional peak at ∼1.99 Å, attributed to the presence of a Pd−O bond, characteristic of partially oxidized Pd/C. In stage 2, this partially oxidized sample was hydrogen purged for 2 h. As a result, the peak attributed to Pd−O disappeared, while a Pd−Pd bond located at ∼2.79 Å increased in intensity, indicating the Pd/C sample is in a metallic state (Pd^0). These changes correspond to coordination number changes for Pd−Pd ($N_{Pd−Pd}$) increasing from 4.25 to 7.08 (Table S1).

In stage 3, the Cu precursor was added and hydrogen purging continued for 6 h to form a surface Cu ultrathin layer, as shown in the FT-EXAFS and XANES spectra. The XANES spectra at the Cu K-edge for the 0.05 M CuCl$_2$ solution (black line), $Pd_{core}Cu_{ultrathin-shell}$/C NPs (red line), and Cu foil reference (green line) are shown in Figure 2C, left. The XANES profile of the Cu precursor, *i.e.*, CuCl$_2$, exhibits a sharp peak at 8995 eV corresponding to the +2 oxidation state.[38] The intensity of this sharp peak (termed a white line), attributed to the 1s → 4p electronic transition, is sensitive to the oxidation state of Cu. After the introduction of a Cu precursor into a suspension of hydrogen-purged NPs, the white line intensity decreased gradually and reached a similar intensity to that of Cu foil, indicating the reduction of Cu^{2+} to Cu^0. After 6 h there was a shift in the edge energy to a lower value (∼3 eV). In addition to a white line feature, a pre-edge feature originating from the 1s → 3d transition[38] is observed at 8980 eV, about 12 eV below the white line peak, which is similar to that of Cu foil. Since the pre-edge peak is a fingerprint for copper metal, its appearance suggests that a Cu ultrathin layer in the metallic state (Cu^0) had been formed. Using EXAFS-based methodology, we have shown that the structure of bimetallic core−shell NPs can be influenced by the atomic distribution between two constituent elements.[39] The same EXAFS-based methodology was used to confirm the formation of the core−shell structure of Pd−Cu NPs. First, we calculated the total number of Pd and Cu atoms around Pd ($\Sigma N_{Pd−i} = N_{Pd−Pd} + N_{Pd−Cu}$) and Cu ($\Sigma N_{Cu−i} = N_{Cu−Cu} + N_{Cu−Pd}$). If $\Sigma N_{Pd−i} > \Sigma N_{Cu−i}$, then the NPs possess a $Pd_{core}−Cu_{shell}$ structure. It was observed that for the NPs $\Sigma N_{Pd−i} > \Sigma N_{Cu−i}$ and $N_{Pd−Pd} > N_{Cu−Cu} > N_{Pd−Cu}$ (see Table S1). It has been shown that for a homogeneous system of A−B bimetallic NPs with a core composed of N atoms of A and a surface made of N atoms of B, the total coordination number for the A atom ($N_{A−i} = N_{A−A} + N_{A−B}$) is greater than the total coordination for the B atom ($N_{B−i} = N_{B−A} + N_{B−B}$).[39] In this case, the interactions at equilibrium follow the order $N_{A−A} > N_{B−B} > N_{A−B}$.[39] Hence, the observed parameter relationships, $\Sigma N_{Pd−i} > \Sigma N_{Cu−i}$ and $N_{Pd−Pd} > N_{Cu−Cu} > N_{Pd−Cu}$, support the $Pd_{core}−Cu_{shell}$ structural assignment for the
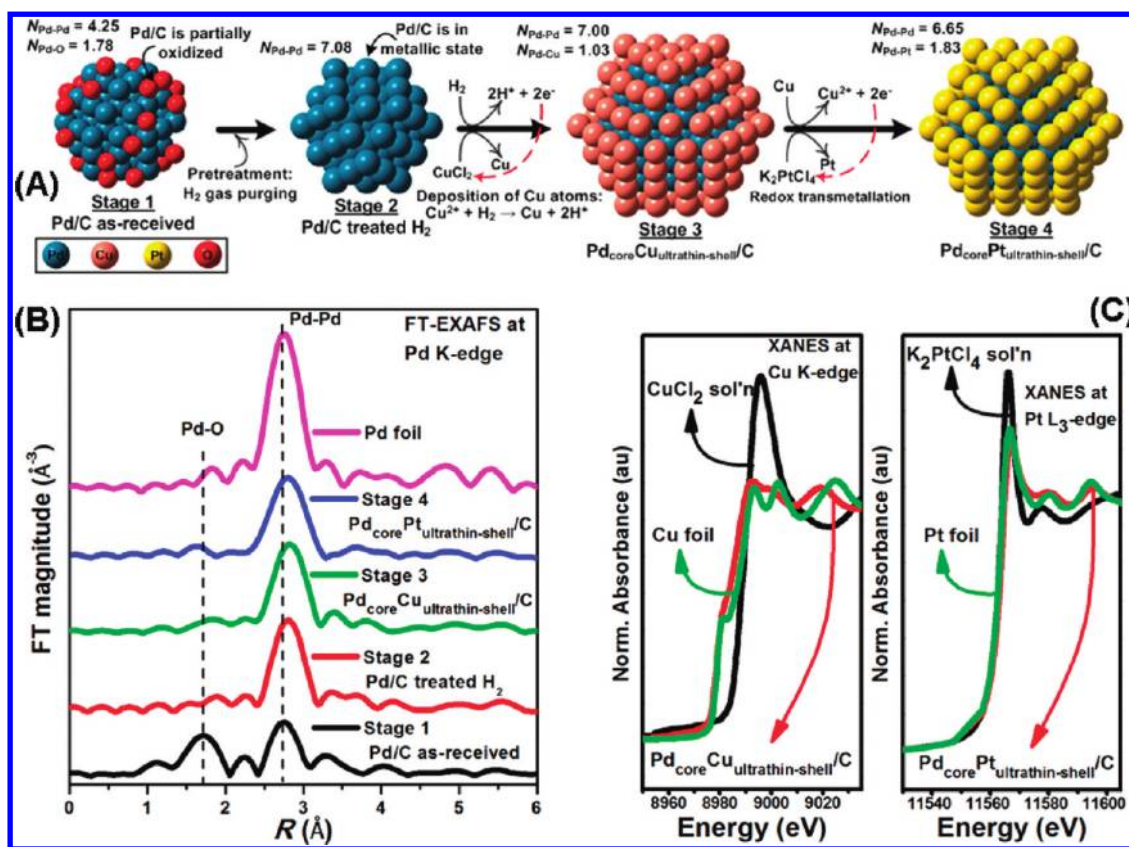
Figure 2. *In situ* X-ray absorption techniques used for probing the reaction mechanism of the Pd$_{core}$Pt$_{ultrathin-shell}$/C NPs. (A) Illustration of the synthesis of Pd$_{core}$Pt$_{ultrathin-shell}$/C NPs based on an electroless method with the corresponding (B) FT-EXAFS spectra at the Pd K-edge for various reaction steps, and (C) XANES spectra at the Cu K- and Pt L$_3$-edges during formation of Pd$_{core}$Cu$_{ultrathin-shell}$/C and Pd$_{core}$Pt$_{ultrathin-shell}$/C NPs, respectively.

Pd$_{core}$Cu$_{ultrathin-shell}$/C NPs. The present method also allows a Cu ultrathin layer to be deposited on other highly reactive noble metal surfaces, *e.g.*, Pt and Ir (see Figure S2). Utilizing these two reactive metals as the core NPs, various core—shell structured NPs such as Pt@Pd, Ir@Pt, and Ir@Pd can be prepared by this general method.

Finally, the Cu ultrathin layer was sacrificially oxidized by the Pt precursor, *i.e.*, K$_2$PtCl$_4$, to form a Pt monolayer on the Pd/C NPs *via* redox—transmetalation. Using the same argument with a Pd$_{core}$—Cu$_{shell}$ structure that was previously confirmed by XAS, we see in Figure 2C, right, that the XANES spectrum for the Pd$_{core}$Pt$_{ultrathin-shell}$/C NPs at the Pt L$_3$-edge is similar to that of Pt foil, indicating a Pt ultrathin layer in a metallic state (Pt^0) had been formed on the Pd/C surface. The observed parameter relationship in Table S1 shows $\sum N_{Pd-i} > \sum N_{Pt-i}$ and $N_{Pd-Pd} > N_{Pt-Pt} > N_{Pd-Pt}$ and confirms the Pd$_{core}$—Pt$_{shell}$ structure of the Pd$_{core}$Pt$_{ultrathin-shell}$/C NPs.

We additionally performed an *in situ* electrochemical analysis to confirm the formation of Cu ultrathin layered Pd/C NPs. The stripping voltammograms of the adsorbed hydrogen and the Cu ultrathin layer are shown in Figure 3A. The striping voltammogram for adsorbed hydrogen on Pd/C was obtained after hydrogen

adsorption (applied potential at 0.00 V), in an electrolyte solution (0.5 M H$_2$SO$_4$) at 30 °C; the potential was scanned at 10 mV·s^{-1}. The stripping curve for the adsorbed hydrogen shows two distinctive desorption peaks in the potential region between 0 and 0.3 V, associated with the oxidation of previously adsorbed hydrogen (2H = 2H$^+$ + 2e$^-$) on different Pd crystalline facets.[40] This suggests that the Pd/C NPs have a strong reactivity toward hydrogen; that is, they absorb, adsorb, split, and oxidize it to generate electrons[22] that can reduce metal ions such as Cu^{2+} and in doing so deposit only a Cu ultrathin layer on the Pd/C NP's surface. The existence of this Cu ultrathin layer correlates well with the stripping voltammogram of the Pd$_{core}$Cu$_{ultrathin-shell}$/C NPs (Figure 3A). The stripping voltammogram was produced as follows: the Pd/C NP's surface was initially treated with hydrogen in a 0.5 M H$_2$SO$_4$ electrolyte solution. Next CuSO$_4$ (0.01 M) was added and the hydrogen purge was continued to ensure that sufficient hydrogen was adsorbed on the NPs to reduce the Cu^{2+} ions to form the sacrificial Cu ultrathin layer.

During the above formation of the sacrificial Cu ultrathin layer, hydrogen is probably absorbed first, then spontaneously diffuses out to the surface of the Pd surface, and subsequently consumed once the Cu^{2+} ions are introduced into the solution, as the ratio of the
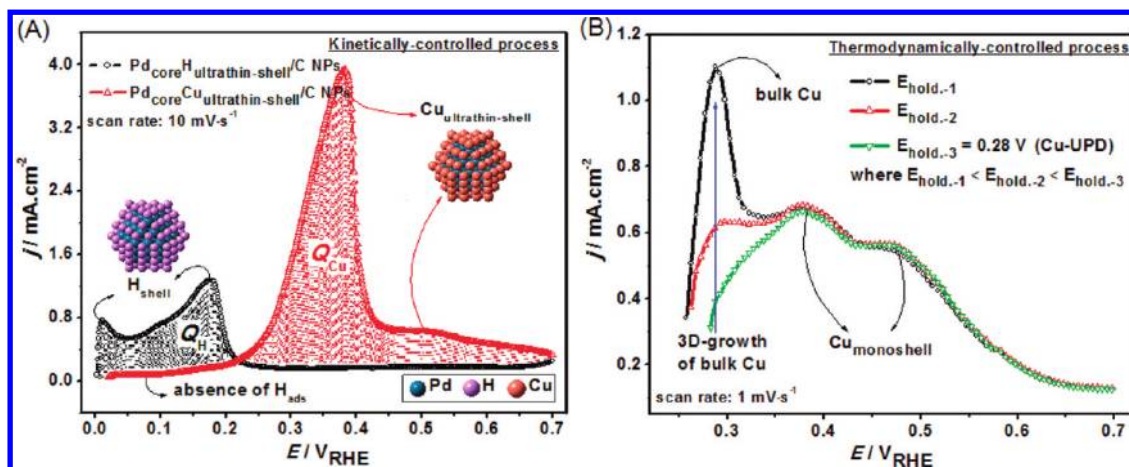
Figure 3. *In situ* electrochemical analysis comparing Cu-deposition processes under kinetically and thermodynamically controlled conditions. (A) Stripping voltammograms of the adsorbed hydrogen monolayer ($-\bigcirc-$) and the adsorbed Cu ultrathin layer ($-\triangle-$) on Pd/C NPs using an electroless method, and (B) stripping voltammograms of the adsorbed Cu layers on Pd/C NPs using electrochemical treatments, *i.e.*, at various applied potentials. Electrolyte: 0.5 M H_2SO_4; temperature: 30 °C.

electron valence of Cu^{2+} to e^- (from dissociated hydrogen) is 2:1. Thus, it is important to constantly purge the hydrogen gas during the synthesis, ensuring a sufficient amount of electron flow from the dissociated hydrogen atoms to complete the layer deposition of Cu atoms and form the Cu ultrathin layer. The situation is different if the hydrogen is not constantly purged, in which case the generated electrons from the dissociated hydrogen would be insufficient to form a complete Cu ultrathin layer.

The Cu^{2+} ions displaced all the adsorbed hydrogen from the NPs' surfaces, which is apparent from the suppression of the hydrogen desorption peaks (Figure 3A). The reduction and deposition of the corresponding Cu^{2+} ions to form a Cu ultrathin layer appear as a strong desorption peak located at ca. 0.38 V.[25] In a previous study, Adzic *et al.*[25] located the stripping Cu-bulk deposition peak, for agglomerated Cu, at a much lower onset potential, 0.21 V, which is different from the value found for the Cu ultrathin layer presented here.

From Figure 3, we also calculated the ratio between the stripping Cu and H charges (Q_{Cu}/Q_H). This determines whether, for this present method, it is possible to form a well-ordered Cu ultrathin layer on the NP's surface, without the three-dimensional (3D) growth of bulk Cu. To quantify Q_H and Q_{Cu}, calculations similar to those reported by Green *et al.*[41] have been used. The Q_{Cu}/Q_H ratio was found to be about 2, a condition where the copper atoms adsorb on the Pd metal surface at the same sites as hydrogen to form a well-ordered Cu ultrathin layer.[41,42]

The cyclic voltammograms (CVs) for the Cu ultrathin layer stripping as a function of deposition time are shown in the supplementary Figure S3. For each stripping, the first CV cycle depicts the stripping curve of the adsorbed Cu atoms on the Pd/C NPs. During the forward step in this first CV cycle [typically after 6 h of

deposition (Figure S3E)], the peak characteristic of bulk absorbed and subsequent adsorbed hydrogen atoms (H_{ads}) was suppressed due to the presence of the adsorbed Cu ultrathin layer (ca. 0.38 V), whereas a peak corresponding to additional growth of Cu-bulk layers was not observed. This Cu ultrathin layer formation was maintained, and importantly no additional growth of Cu bulk was formed, even after the reaction was extended up to 8 h (Figure S3F). On the second sweep, performed after stripping Cu, the voltammograms mirrored those observed for Pd/C NPs (*i.e.*, the absence of adsorbed Cu). These results emphasize the viability of the present method in achieving only a Cu ultrathin layer deposition on a Pd core surface.

For comparison we conducted a parallel study in which the Cu layers were deposited on a Pd/C surface using an electrochemical (UPD) method, in which holding potentials were employed, to deposit Cu layers in a thermodynamically controlled reaction. A Cu monolayer can be formed at a holding potential of 0.28 V (E_{hold-3}), as indicated with black arrows (Figure 3B). However, the holding potential associated with this Cu-UPD monolayer must be determined carefully; otherwise it may form an incomplete Cu-UPD monolayer and/or additional bulk Cu deposits.[41] For example, a slight change in the holding potential to a lower value, *e.g.*, E_{hold-1} and E_{hold-2}, triggers the growth of additional bulk Cu, as indicated by the strong peak located at ca. 0.28 V.

For the reduction reaction of $Cu^{2+} + 2e^- \rightarrow Cu_{(s)}$ at standard conditions, the bulk $Cu_{(s)}$ will be deposited at the equilibrium potential ($E_{bulk-Cu}$) of 0.3402 V, in accordance with the Nernst equation:

$$E_{bulk-Cu} = E_{Cu}^0 + \frac{RT}{nF}\ln[C_{Cu^{2+}}] \quad (1)$$

where $E_{Cu}^0 = 0.3402$ V, $R = 8.31441$ J·mol^{-1}·K^{-1}, $F = 96484.6$ C·mol^{-1}, $C_{Cu^{2+}} = 1$ M, and $n = 2$, at a temperature (T) of 298 K. In general, when the Cu^{2+} concentration is

less than under standard conditions ($C_{Cu^{2+}}$ = 1 M), the equilibrium will shift to the left. This means that the equilibrium potential ($E_{bulk-Cu}$) for the bulk-Cu deposition will shift to negative. Our experiments in the present study used a Cu solution, *i.e.*, $C_{Cu^{2+}}$, at the concentration 0.01 M and a temperature (*T*) of 303 K (30 °C), which leads to bulk-Cu deposition at the equilibrium potential ($E_{bulk-Cu}$) of 0.28 V. It is noteworthy that the peak associated with the bulk-Cu deposition in Figure 3B, which is located at 0.28 V, matches that predicted from the Nernst equation.

The same Pd/C catalyst was also used to perform a kinetically controlled Cu ultrathin layer deposition (Figure 3A and Figure S3): it was found that a strong desorption peak associated with the Cu ultrathin layer was located at *ca.* 0.38 V, similar with that of a thermodynamic Cu-UPD process (Figure 3B).

The present kinetically controlled method achieves the formation of a Cu ultrathin layer and overcomes the problem of the 3D growth of bulk Cu associated with the thermodynamically controlled electrochemical method. In our previous study,[43] two principle reaction mechanisms were proposed to account for the autocatalytic reduction process: the first is a chemical mechanism, while the second is an electrochemical mechanism. In the chemical mechanism, there are two proposed explanations. The first is the "atomic hydrogen mechanism" proposed by Brenner and Riddle, while the second is the "hydride ion mechanism" proposed by Hersch. In this chemical mechanism, a kinetically controlled reaction is envisioned to take place because the Pd surface is the only catalytically active site for the adsorption of hydrogen and/or the hydride that can be used for reducing and depositing Cu atoms, whereas the predeposited Cu atoms are not an active site for this mechanism and thus restrict the growth of Cu layers on this predeposited Cu surface. This sort of kinetically controlled reaction in the chemical mechanism is also consistent with a previous discussion on DFT results in Figure 1. Meanwhile, if the Cu deposition is based on an electrochemical mechanism, some Cu atoms are probably also deposited on the previously formed Cu layer since the electrons can go through everywhere in this mechanism. However, using the DFT data presented in Supplementary Figure S4 and Table S2, this possibility can be ruled out, since the binding energy of Pd—Cu (−8.88 eV) is much stronger than that of the Cu—Cu (−5.58 eV) interaction; thus the Cu atoms preferred deposition on the Pd-core surface as a Cu ultrathin layer. This means no matter which mechanism, either the chemical or electrochemical mechanism, is involved in the process, Cu ultrathin layer deposition on the Pd-core surface can always be obtained. This is also consistent with the experimental results.

The Cu ultrathin layer was then used to form a Pt ultrathin layer on the Pd/C NPs, and the resulting material was characterized using *in situ* electrochemical FTIR
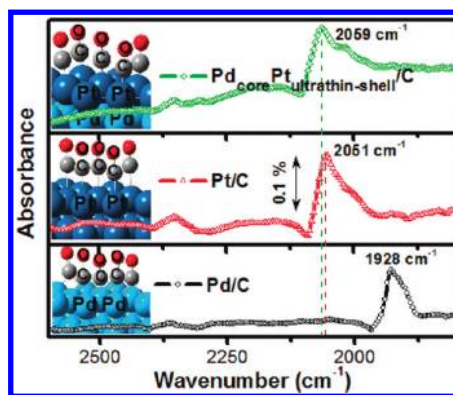

Figure 4. FTIR spectra of (—○—) Pd/C, (—△—) Pt/C, and (—◇—) Pd$_{core}$Pt$_{ultrathin-shell}$/C NPs with the adsorption of CO at 0.05 V recorded using a spectral resolution of 8 cm^{-1} in 0.1 M HClO$_4$. Inset: multiadsorbed CO molecules on the slab system constructed by the DFT modeling.

(EC-FTIR) measurements. The FTIR spectra for the Pd/C, Pt/C, and Pd$_{core}$Pt$_{ultrathin-shell}$/C NPs samples were recorded after the CO adsorption at 0.05 V (Figure 4). A strong band at 1928 cm^{-1} was attributed to the stretching of bridged CO adsorbed on the surface of the Pd/C catalyst. In contrast, the Pt/C catalyst shows a strong band at 2051 cm^{-1}, attributed to an adsorbed linear CO. These FTIR-CO spectra are consistent with the reported Pd and Pt studies.[22,23] It is noteworthy that in the case of the Pd$_{core}$Pt$_{ultrathin-shell}$/C catalyst the covering of the Pt ultrathin shell on the Pd core gave similar results to Pt/C, where a linear CO adsorption band on the Pt ultrathin shell appeared at 2059 cm^{-1}. The band, associated with CO adsorbed on Pd at 1928 cm^{-1}, completely disappeared, proving that the Pd core was completely covered by a Pt shell. In agreement with the FTIR-CO results, our DFT modeling study based on the slab system verified the differences in the stretching frequencies of the adsorbed CO (see Table S3). After applying energy minimization, the corresponding CO adsorption energies and geometric properties are also consistent with previously reported DFT studies.[28,44,45] Taken together, DFT modeling and data from the FTIR-CO probe confirm that a Pd$_{core}$Pt$_{ultrathin-shell}$/C NPs structure is formed.

The synthesized Pd$_{core}$Pt$_{ultrathin-shell}$/C NPs were found to be spherically shaped and reasonably well dispersed with an average size of 4.5 nm (inset in Figure 5A). The spherical shape homogeneity of the NPs was maintained by depositing the Pt atoms only on the top of the Pd core. It is important to note that the self-nucleation of an additional thick Pt layer was averted and that only a uniform Pt ultrathin layer on the Pd/C NPs surface was generated. Recently, TEM has been successfully utilized for the characterization of a single core—shell particle, *i.e.*, a Pd—Pt core—shell nanoplate with an edge length of over 50 nm.[46] However, the use of TEM is still limited by the low detector collection efficiency, especially for small bimetallic NPs (<5 nm), where the electron dosage required for successful TEM
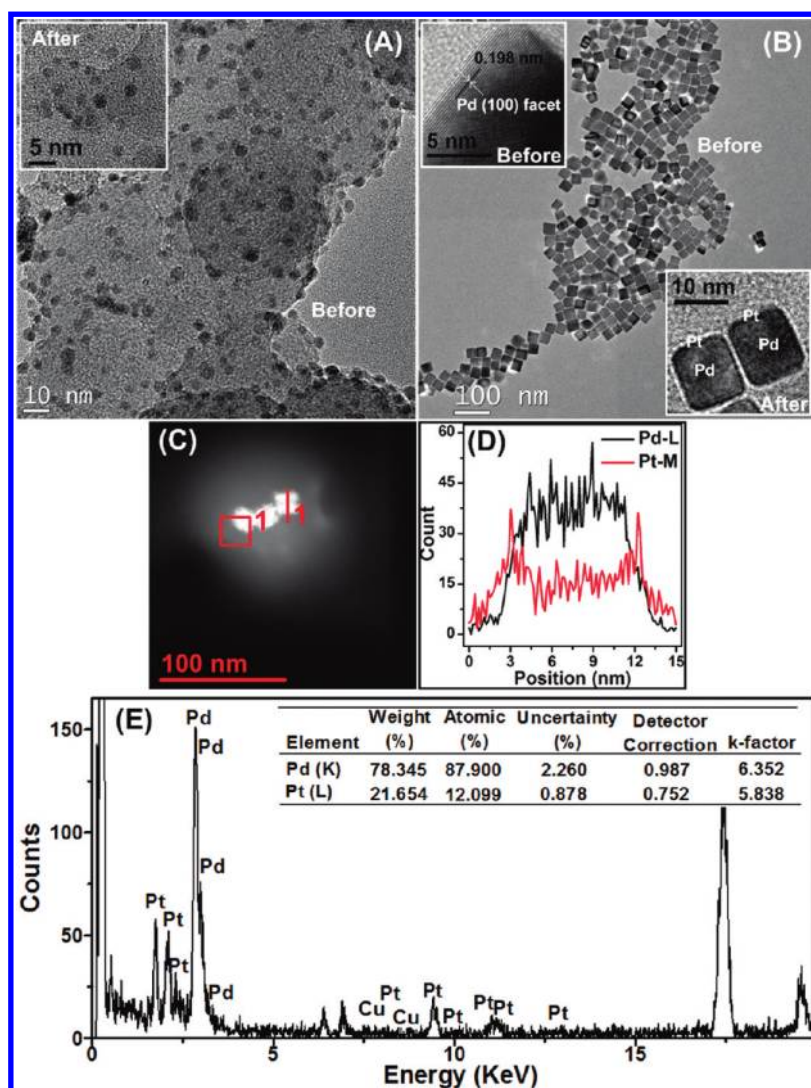
Figure 5. TEM images of the synthesized (A) Pd/C spherical and (B) Pd cubic NPs. Inset: Their corresponding images after the deposition of a Pt ultrathin layer on Pd NPs with a different shape. (C) HAADF-STEM images of cubic-shaped $Pd_{core}Pt_{ultrathin-shell}$, (D) its line profile analysis along line 1 in panel C, and (E) its EDX spectrum together with the corresponding bimetallic Pd:Pt atomic composition results.

analysis is often too high and beyond the radiation damage thresholds of the NPs,[47] and this may also change the NPs' position. To demonstrate the viability of the present strategy, we used Pd nanocubes (~10 nm), adopting a method proposed by Xia et al.[48] As can be seen from Figure 5B, these cubic NPs comprising a Pd(100) facet were uniformly covered with a relatively darker colored ultrathin shell of Pt and clearly not nucleated Pt-NPs, which also indicates the formation of well-defined core−shell structure. From the HAADF-STEM image (Figure 5C), a line-profile analysis was performed, the results of which, presented in Figure 5D, show that the thickness of the Pt shell was approximately 0.3 nm, which is close to the thickness of a Pt ultrathin layer. The corresponding EDX spectrum (Figure 5E) shows a Pd:Pt atomic ratio of around 7.27:1, which is close to the theoretical value (8:1) for the cubic Pd_{core} $Pt_{ultrathin-shell}$ NPs with a size of around 10 nm. In

addition, STEM-EDX measurements on the Cu monolayer on the Pd nanocube were performed (see supplementary Figure S5). It is clear that the line profile of this $Pd_{core}Cu_{ultrathin-shell}$ cubic sample demonstrates a similarity to the core-monolayered shell structure of the Pd−Pt system. The thickness of the Cu shell is also approximately 0.3 nm, thus indicating a Cu ultrathin layer was formed using our strategy.

In order to examine if the redox−transmetalation reaction of Cu by Pt is complete, XANES measurements particularly at the Cu K-edge were performed, and it was found that the as-prepared spherical-shaped Pd@Pt/C NPs contain only an insignificant quantity of 2.3% Cu residues (Figure S6) that can be easily removed by a simple electrochemical treatment, i.e., a repetitive cycling treatment for 10 cycles with a scan range of 0.00 to 1.05 V_{RHE} at a scan rate of 0.05 $V \cdot s^{-1}$ in 0.5 M H_2SO_4 electrolyte solution. This electrochemical treatment
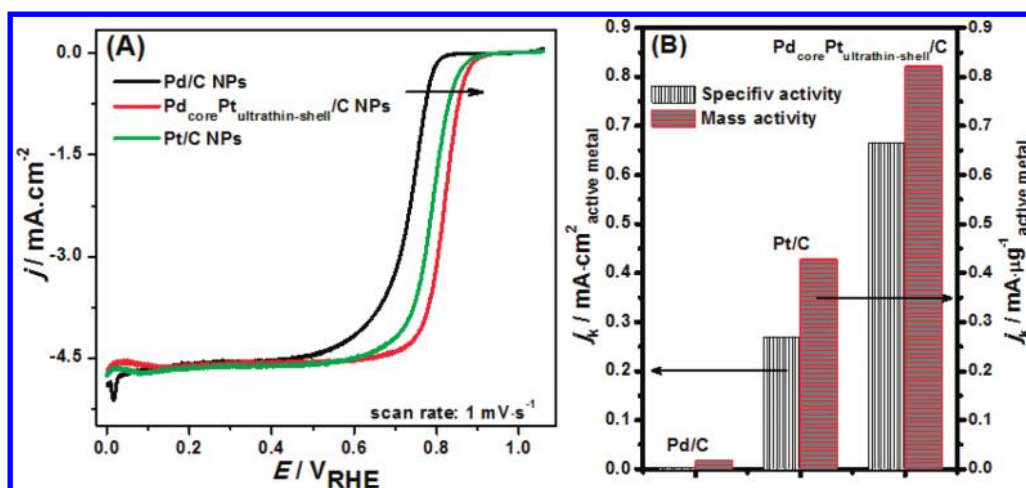
Figure 6. (A) Example of the application of the $Pd_{core}Pt_{ultrathin-shell}$/C NPs: an oxidation reduction reaction in hydrogen fuel cells, showing the corresponding linear scan voltammograms (LSVs) recorded at 1 mV·s^{-1} for this reaction at 1600 rpm in an oxygen-saturated 0.5 M H_2SO_4 solution. (B) Mass and specific activities for the $Pd_{core}Pt_{ultrathin-shell}$/C NPs in comparison with their countermetallic Pd/C and Pt/C commercial catalysts.

has also been employed in the surface-sensitive-based techniques, *i.e.*, cyclic voltammograms measurements. From these cyclic voltammograms (Figure S7A), we did not find any trace of Cu residues, since the anodic and cathodic peak currents, at a potential range of approximately 0.3−0.6 V, corresponding to the presence of Cu were not observed. These findings indicate that the redox−transmetalation process with subsequent minor electrochemical treatments is exceptionally effective in replacing the Cu layer to form a Pt layer on the Pd core. A similar observation was also made by Adzic *et al.*,[24] who also employed an electrochemical treatment, *i.e.*, a linear potential sweep with a scan range up to 1.00 V$_{RHE}$, after the redox−transmetalation reaction of Cu by Pt. They also found that the Cu layer can be completely displaced by this combined redox−transmetalation and subsequent electrochemical processing. To give clear evidence of the viability of the present strategy, we strictly performed TEM-EDX measurements using Cu-free grids (*i.e.*, Mo grid) for the sample of the prepared spherical-shaped Pd@Pt/C NPs and electrochemically treated Pd@Pt/C NPs. It is noteworthy that our findings in EDX analyses are in good agreement with our findings on XANES and electrochemical measurements, where the insignificant 2.9% Cu residues (Figure S8A) can be completely removed from the sample (Figure S8B).

We have also performed TEM measurements with a larger area (low-magnification) for the Pd@Pt NPs with both the spherical and cubic shapes and provided their particle size distributions. The particle size of the spherical and cubic Pd@Pt NPs is found to be uniform around 10.7 and 4.5 nm, respectively (Figure S9). In addition, the TEM image for the cubic Pd@Pt NPs shows that the Pd-core surface was uniformly covered with a Pt ultrathin layer. We also performed

powder-XRD measurements for both the spherical- and cubic-shaped Pd@Pt NPs (Figure S10) and found a size similarity to that from TEM measurements. To be specific, the particle size of the spherical and cubic Pd@Pt NPs, estimated by the Scherrer's equation, is found to be 10.6 and 4.3 nm, respectively. Additionally in particular with the cubic-shaped Pd@Pt NPs, we found two important main peaks located at ∼39° and ∼46°, which represent the (111) and (100) facets, respectively. The presence of a strong (100) facet in addition to the (111) facet indicates the existence of a cubic shape for this particular Pd@Pt sample.

Figure 6 shows comparisons with carbon-based counterparts, *i.e.*, the commercial BASF Pd/C and E-tek Pt/C NPs (20 wt %). The data presented in Figure 6A have been normalized to the geometric area of the rotating disk electrode (0.1964 cm^2), where all the electrochemical measurements used the same weight loading of an active metal, *i.e.*, 0.22 mg·cm^{-2}. In particular for $Pd_{core}Pt_{ultrathin-shell}$/C NPs, the calculation is based on their active Pt metal shell. Mass and specific activities at 0.9 V$_{RHE}$ are given as kinetic current density (j_k) normalized in reference to the weight loading amount and the electrochemically active surface area (ECSA) of an active metal, respectively.

The intrinsic ORR activities, both mass and specific activities (j_k) for the Pd/C, Pt/C, and $Pd_{core}Pt_{ultrathin-shell}$/C NPs under similar experimental conditions, were calculated on the basis of the LSVs curves (Figure 6A). In practice the j_k value was calculated from the ORR-LSVs curve by using mass-transport correction and normalized to the weight loading amount and the ECSA of an active metal in order to compare the mass and specific activities of the NPs, respectively (the detailed steps of the calculation are provided in

the Supporting Information). The corresponding results are presented in Figure 6B. It can be seen that $Pd_{core}Pt_{ultrathin-shell}$/C NPs show an enhancement in both mass and specific activities compared to Pd/C and Pt/C. To be specific, the $Pd_{core}Pt_{ultrathin-shell}$/C NPs exhibited a specific activity of 665 $\mu A \cdot cm^{-2}$ at 0.9 V, which is more than double that for Pt/C (268 $\mu A \cdot cm^{-2}$) and almost 20 times that for the Pd/C (37.5 $\mu A \cdot cm^{-2}$). For a mass activity, a similar tendency is observed, where its sequence follows the order $Pd_{core}Pt_{ultrathin-shell}$/C > Pt/C > Pd/C. In this study, the measured mass and specific activities for this sort of Pt-monolayered nanostructure are in good agreement with the reported values in the literature, *e.g.*, Adzic *et al.*'s work.[24]

The sequence in the mass and specific activities is also consistent with the results from the cyclic voltammograms (Figure S7), where the Pt ultrathin layer shifts the onset of metal-oxide formation and oxide reduction (indicated with arrows) to more positive potentials compared to the Pd/C NPs, indicating that a Pt ultrathin layer inhibits surface chemisorption of oxygenated species at high potentials[25] and could lead to an enhancement in ORR kinetics.[49,50] Reducing the Pt content of the cathode electrocatalyst while increasing the activity of Pt ultrathin layered NPs makes this particular Pt ultrathin layered nanostructure a very promising solution to one of the major problems of existing fuel cell technology.

CONCLUSION

We have shown that the present kinetically controlled autocatalytic chemical process can be effectively used as a general protocol for the fabrication of well-defined bimetallic core@shell structured NPs, such as Pd@Pt, Pt@Pd, Ir@Pt, and Ir@Pd. The presented method, which utilizes the strong reducing ability of the adsorbed hydrogen on the surface of noble metals, can reduce the Cu precursors and subsequently form only a Cu ultrathin layer on these metals' surfaces. This is because the Cu ultrathin layer is inactive toward hydrogen and so can restrict the self-nucleation of additional thick Cu atom layers. This sort of kinetically controlled synthesis has been clearly described in our first-principles DFT calculations, and it elegantly overcomes the drawbacks of the conventional thermodynamically controlled electrochemical (*i.e.*, UPD) method, namely, its limited production capacity. The resulting Cu ultrathin layer was sacrificially oxidized to form another metal ultrathin layer shell through the redox process. The selected core−shell NPs with their multifunctionalities and enhanced properties have been tested in one particularly critical catalytic reaction, this being the oxygen reduction reaction in hydrogen fuel cells.

METHODS

Materials. Commercial Pd/C (20 wt %) catalyst was purchased from BASF Fuel Cell Inc. and used as the core material. The Cu and Pt precursor salts, *i.e.*, K_2PtCl_4 and $CuCl_2 \cdot 2H_2O$, were purchased from Alfa Aesar. The ethanol (HPLC grade) was purchased from Sigma Aldrich and used as received.

Synthesis of $Pd_{core}Pt_{ultrathin-shell}$/C Catalyst. The synthesis procedure was initiated by sonicating 0.266 g of Pd/C catalyst in 50 mL of mixed solvent [ethanol−water (1:1)] for 1 h to form a uniform suspension. This Pd/C suspension was then treated with H_2 gas under constant stirring for 2 h. Later, an aqueous solution of 50 mL of 5×10^{-3} M $CuCl_2$ was added into the reaction flask containing a pretreated Pd/C suspension and stirred for 6 h under constant H_2 gas purging. The resulting nanoparticles were then isolated from their solvent using a high-power centrifugal pump (20 000 rpm for 30 min) and redispersed in 50 mL of ethanol−water (1:1). Into this suspension was added an aqueous solution of 50 mL of 5×10^{-3} M K_2PtCl_4 at a flow rate of 1 mL/min. The reaction temperature was raised to 60 °C at a heating rate of 5 °C/min and maintained for another 6 h under a N_2 atmosphere using a standard airless technique. Finally, the resulting product was washed by centrifugation and then dried at 80 °C in an air oven for about 8 h.

In Situ EC-FTIR Measurements. A conventional three-electrode electrochemical cell with a high surface area Pt counter electrode and a saturated calomel electrode (SCE) reference electrode, powered by a Solartron 1480 potentiostat/galvanostat, was used. The working electrode was made of the catalyst slurry with a loading of 37 μg of catalyst/cm^2 immobilized on a polished Au surface (diameter of 1.3 cm) as described in our previous report.[28] Prior to the measurements, Ar gas was purged into 0.1 M $HClO_4$ electrolyte solution for 30 min, following which 10 cycles of continuous cyclic voltammograms (potential range 0.00−1.00 V_{RHE}) were subsequently applied to the catalyst. CO adsorption on the catalyst's surface was carried out by holding the potential at 0.05 V and simultaneously purging CO gas into this $HClO_4$ solution for 30 min. Next the dissolved CO was removed by purging with N_2 gas for 15 min, and the corresponding infrared spectrum for the adsorbed CO was recorded afterward. The FTIR spectra were recorded using the infrared end-station of a Thermo-Fisher-Nicolet Magna 860 spectrometer equipped with an MCT/A detector at the beamline BL14A1 of National Synchrotron Radiation Research Center (NSRRC), Hsinchu, Taiwan. The configuration of the spectro-electrochemical cell for this study was similar to that described in our previous report.[28]

TEM and in Situ XAS Measurements. A FEI-TEM-2000 microscope was used in the TEM measurement and was operated at an accelerating voltage of 3800 kV. Specimens were prepared by ultrasonically suspending the nanoparticles in ethanol, which were then applied to a molybdenum (Mo) grid and dried in air. The XAS spectra were recorded at the Taiwan Beamline of BL07A1 and at BL01C1 at the NSRRC, Hsinchu, Taiwan. The electron storage ring of the NSRRC was operated at 1.5 GeV. A double Si(111) crystal monochromator was employed for energy selection with a resolution $\Delta E/E$ better than 1×10^{-4} at the Pt L_3 (11564 eV), Cu K (8979 eV), and Pd K (24350 eV) edges. All the spectra were recorded at room temperature in transmission mode. Three gas-filled ionization chambers were used in series to measure the intensities of the incident beam (I_0), the beam transmitted by the sample (I_t), and the beam subsequently transmitted by the reference foil (I_r). The third ion chamber was used in conjunction with the reference samples, which were a Pt foil, a Cu foil, and a Pd foil for the Pt L_3-, Cu K-, and Pd K-edge measurements, respectively. The control of parameters for EXAFS measurements, data collection modes, and calculation of errors was all done as per the guidelines set by the International XAFS Society Standards and Criteria Committee.[51,52]

Computation Methodology. We employed the projector-augmented waves (PAW)[53−55] generalized gradient approximation

(GGA)[56,57] as implemented in the Vienna *ab initio* simulation package (VASP).[58-60] In the plane wave calculation, a cutoff energy of 300 eV was applied for all the slab systems. Each slab system consists of four layers with four atoms per layer. The surface is constructed as a slab within the three-dimensional periodic boundary conditions, and models are separated from their images in the direction perpendicular to the surface by a 14 Å vacuum layer. The bottom layer was kept fixed to the bulk coordinates; full atomic relaxations were allowed for the top three layers. For these calculations, a $7 \times 7 \times 1$ k-point mesh was used in the 3×3 supercell. The atoms in the cell were allowed to relax until the forces on unconstrained atoms were less than 0.05 eV Å^{-1}.

Electrode Preparation and Electrochemical Measurements. Millipore water (18 MΩ) and sulfuric acid (Across) were used. All experiments were carried out at an ambient temperature of 30 ± 1 °C. A conventional three-electrode electrochemical cell was used for the electrochemical measurements, with a high surface area Pt counter electrode and a SCE reference (all potentials in this paper are quoted *vs* the RHE electrode), powered by a Solartron (1480 model) potentiostat/galvanostat. The working electrode was made of the carbon-supported Pt, Pd, and Pd$_{core}$Pt$_{monoshell}$ NPs immobilized on a glassy carbon electrode (GCE) surface. The procedure for the electrode fabrication involved, first, the preparation of a clear suspension by sonicating a known amount of NP powder dispersed in 0.5% Nafion; second, placing an aliquot of the suspension (7 μL of 6.2 μg$_{Pt}$·mL^{-1} of the catalyst) on the GCE disk; and third air-drying about 5 min at room temperature and then at 80 °C to yield a uniform thin film of the catalyst. Sulfuric acid (0.5 M) was used as a supporting electrolyte for all the experiments. After fabrication the electrodes were immersed in 200 mL of N$_2$-saturated 0.5 M sulfuric acid, and the potential was scanned from 0.00 to 1.05 V$_{RHE}$ about 10 cycles at a scan rate of 0.05 V·s^{-1} for the pretreatment. The cyclic voltammogram experiments were performed at a scan rate of 10 mV·s^{-1} with a scan range 0.00–1.05 V$_{RHE}$. For the ORR experiments, the same electrolyte solution was initially purged with O$_2$ gas for 30 min. After this, the LSVs for the ORR were recorded by sweeping the potential from 0.00 to 1.05 V at 1 mV·s^{-1} at a rotation speed of 1600 rpm. Meanwhile the detailed steps of calculation for the ECSA and intrinsic ORR activity, *i.e.*, mass and specific activities, are provided in the Supporting Information.

Supporting Information Available: Results showing the FT-EXAFS spectra of the experimental and two-shell fitting data at various reaction steps during the formation of the Pd$_{core}$-Pt$_{ultrathin-shell}$/C NPs (Figure S1) with their corresponding structural parameters (Table S1), Cu K-edge XANES spectra for the deposition of Cu ultrathin layer on the surface of various noble metal NPs, *e.g.*, Pt/C and Ir/C (Figure S2), CVs in the *in situ* stripping of the adsorbed Cu ultrathin layer on Pd/C NPs, as a function of time (Figure S3), DFT modeling of a Cu atom deposition on Pd(111) and Cu(111) slab surfaces (Figure S4) with their corresponding binding energies (Table S2), HAADF-STEM images of Pd$_{core}$-Cu$_{ultrathin-shell}$ cubic shape with its line-profile analysis and EDX spectrum (Figure S5), XANES spectra of the as-prepared spherical-shaped Pd$_{core}$Pt$_{ultrathin-shell}$/C NPs at the Pd K-, Cu K-, and Pt L$_3$-edges (Figure S6), cyclic voltammograms for a Pt ultrathin layer on Pd/C NPs obtained *via* redox displacement of Cu ultrathin layer compared with those of monometallic Pd/C and Pt/C counterparts (Figure S7A), together with their corresponding ECSA values (Figure S7B), stretching properties of the adsorbed CO on Pd (111), Pt (111), and Pt$_{monoshell}$Pd$_{core}$ (111) slab systems calculated from DFT modeling (Table S3), EDX spectra of the as-prepared and electrochemically treated spherical-shaped Pd$_{core}$Pt$_{ultrathin-shell}$/C NPs together with their corresponding Pd:Pt:Cu atomic composition (Figure S8), TEM images of the spherical- and cubic-shaped Pd$_{core}$Pt$_{ultrathin-shell}$ NPs (Figure S9), and XRD patterns of the spherical- and cubic-shaped Pd$_{core}$Pt$_{ultrathin-shell}$ NPs (Figure S10) are available free of charge *via* the Internet at http://pubs.acs.org.

REFERENCES AND NOTES

1. Greeley, J.; Stephens, I. E. L.; Bondarenko, A. S.; Johansson, T. P.; Hansen, H. A.; Jaramillo, T. F.; Rossmeisl, J.; Chorkendorffl; Nørskov, J. K. Alloys of Platinum and Early Transition Metals as Oxygen Reduction Electrocatalysts. *Nat. Chem.* **2009**, *1*, 552–556.
2. Stamenkovic, V. R.; Fowler, B.; Mun, B. S.; Wang, G.; Ross, P. N.; Lucas, C. A.; Marković, N. M. Improved Oxygen Reduction Activity on Pt$_3$Ni(111) *via* Increased Surface Site Availability. *Science* **2007**, *315*, 493–497.
3. Alloyeau, D.; Ricolleau, C.; Mottet, C.; Oikawa, T.; Langlois, C.; Le Bouar, Y.; Braidy, N.; Loiseau, A. Size and Shape Effects on the Order-Disorder Phase Transition in CoPt Nanoparticles. *Nat. Mater.* **2009**, *8*, 940–946.
4. Sato, K. Magnetic Nanoparticles: When Atoms Move Around. *Nat. Mater.* **2009**, *8*, 924–925.
5. Cao, A.; Veser, G. Exceptional High-temperature Stability through Distillation-like Self-Stabilization in Bimetallic Nanoparticles. *Nat. Mater.* **2010**, *9*, 75–81.
6. Seo, W. S.; Lee, J. H.; Sun, X.; Suzuki, Y.; Mann, D.; Liu, Z.; Terashima, M.; Yang, P. C.; McConnell, M. V.; Nishimura, D. G.; *et al*. FeCo/Graphitic-Shell Nanocrystals as Advanced Magnetic-Resonance-Imaging and Near-Infrared Agents. *Nat. Mater.* **2006**, *5*, 971–976.
7. Reiss, G.; Hutten, A. Magnetic nanoparticles: Applications beyond Data Storage. *Nat. Mater.* **2005**, *4*, 725–726.
8. Park, J.-I.; Cheon, J. Synthesis of "Solid Solution" and "Core-Shell" Type Cobalt–Platinum Magnetic Nanoparticles *via* Transmetalation Reactions. *J. Am. Chem. Soc.* **2001**, *123*, 5743–5746.
9. Lee, W. R.; Kim, M. G.; Choi, J. R.; Park, J. I.; Ko, S. J.; Oh, S. J.; Cheon, J. Redox–Transmetalation Process as a Generalized Synthetic Strategy for Core–Shell Magnetic Nanoparticles. *J. Am. Chem. Soc.* **2005**, *127*, 16090–16097.
10. Zhang, S.; Lopez, F. J.; Hyun, J. K.; Lauhon, L. J. Direct Detection of Hole Gas in Ge–Si Core–Shell Nanowires by Enhanced Raman Scattering. *Nano Lett.* **2010**, *10*, 4483–4487.
11. Zhang, J.; Sasaki, K.; Sutter, E.; Adzic, R. R. Stabilization of Platinum Oxygen-Reduction Electrocatalysts Using Gold Clusters. *Science* **2007**, *315*, 220–222.
12. Zhang, J.; Vukmirovic, M. B.; Xu, Y.; Mavrikakis, M.; Adzic, R. R. Controlling the Catalytic Activity of Platinum-Monolayer Electrocatalysts for Oxygen Reduction with Different Substrates. *Angew. Chem., Int. Ed.* **2005**, *117*, 2170–2173.
13. Sasaki, K.; Naohara, H.; Cai, Y.; Choi, Y. M.; Liu, P.; Vukmirovic, M. B.; Wang, J. X.; Adzic, R. R. Core-Protected Platinum Monolayer Shell High-Stability Electrocatalysts for Fuel-Cell Cathodes. *Angew. Chem., Int. Ed.* **2010**, *49*, 8602–8607.
14. Yam, V. W. W. Behind Platinum's Sparkle. *Nat. Chem.* **2010**, *2*, 790.
15. Schmid, G.; Lehnert, A.; Malm, J.-O.; Bovin, J.-O. Ligand-Stabilized Bimetallic Colloids Identified by HRTEM and EDX. *Angew. Chem., Int. Ed. Engl.* **1991**, *30*, 874–876.
16. Lim, B.; Lu, X.; Jiang, M.; Camargo, P. H. C.; Cho, E. C.; Lee, E. P.; Xia, Y. Facile Synthesis of Highly Faceted Multioctahedral Pt Nanocrystals through Controlled Overgrowth. *Nano Lett.* **2008**, *8*, 4043–4047.
17. Fang, B.; Chaudhari, N. K.; Kim, M.-S.; Kim, J. H.; Yu, J.-S. Homogeneous Deposition of Platinum Nanoparticles on Carbon Black for Proton Exchange Membrane Fuel Cell. *J. Am. Chem. Soc.* **2009**, *131*, 15330–15338.
18. Peng, Z.; Yang, H. Synthesis and Oxygen Reduction Electrocatalytic Property of Pt-on-Pd Bimetallic Heteronanostructures. *J. Am. Chem. Soc.* **2009**, *131*, 7542–7543.
19. Lim, B.; Jiang, M.; Camargo, P. H. C.; Cho, E. C.; Tao, J.; Lu, X.; Zhu, Y.; Xia, Y. Pd-Pt Bimetallic Nanodendrites with High Activity for Oxygen Reduction. *Science* **2009**, *324*, 1302–1305.

20. Habas, S. E.; Lee, H.; Radmilovic, V.; Somorjai, G. A.; Yang, P. Shaping Binary Metal Nanocrystals through Epitaxial Seeded Growth. *Nat. Mater.* **2007**, *6*, 692–697.

21. Lee, H.; Habas, S. E.; Somorjai, G. A.; Yang, P. Localized Pd Overgrowth on Cubic Pt Nanocrystals for Enhanced Electrocatalytic Oxidation of Formic Acid. *J. Am. Chem. Soc.* **2008**, *130*, 5406–5407.

22. Wang, Y.; Toshima, N. Preparation of Pd–Pt Bimetallic Colloids with Controllable Core/Shell Structures. *J. Phys. Chem. B* **1997**, *101*, 5301–5306.

23. Toshima, N.; Shiraishi, Y.; Shiotsuki, A.; Ikenaga, D.; Wang, Y. Novel Synthesis, Structure and Catalysis of Inverted Core/Shell Structured Pd/Pt Bimetallic Nanoclusters. *Eur. Phys. J. D* **2001**, *16*, 209–212.

24. Wang, J. X.; Inada, H.; Wu, L.; Zhu, Y.; Choi, Y.; Liu, P.; Zhou, W.-P.; Adzic, R. R. Oxygen Reduction on Well-Defined Core–Shell Nanocatalysts: Particle Size, Facet, and Pt Shell Thickness Effects. *J. Am. Chem. Soc.* **2009**, *131*, 17298.

25. Zhang, J.; Mo, Y.; Vukmirovic, M. B.; Klie, R.; Sasaki, K.; Adzic, R. R. Platinum Monolayer Electrocatalysts for O$_2$ Reduction: Pt Monolayer on Pd(111) and on Carbon-Supported Pd Nanoparticles. *J. Phys. Chem. B* **2004**, *108*, 10955–10964.

26. Sasaki, K.; Wang, J. X.; Naohara, H.; Marinkovic, N.; More, K.; Inada, H.; Adzic, R. R. Recent Advances in Platinum Monolayer Electrocatalysts for Oxygen Reduction Reaction: Scale-up Synthesis, Structure and Activity of Pt Shells on Pd Cores. *Electrochim. Acta* **2010**, *55*, 2645–2652.

27. Yamauchi, M.; Kobayashi, H.; Kitagawa, H. Hydrogen Storage Mediated by Pd and Pt Nanoparticles. *ChemPhysChem* **2009**, *10*, 2566–2576.

28. Lin, Y. C.; Chou, H. L.; Tsai, M. C.; Hwang, B. J.; Sarma, L. S.; Lee, Y. C.; Chen, C. I. Combined Experimental and Theoretical Investigation of Nanosized Effects of Pt Catalyst on Their Underlying Methanol Electro-Oxidation Activity. *J. Phys. Chem. C* **2009**, *113*, 9197–9205.

29. Lai, F.-J.; Chou, H.-L.; Sarma, L. S.; Wang, D.-Y.; Lin, Y.-C.; Lee, J.-F.; Hwang, B.-J.; Chen, C.-C. Tunable Properties of Pt$_x$Fe$_{1-x}$ Electrocatalysts and Their Catalytic Activity towards the Oxygen Reduction Reaction. *Nanoscale* **2010**, *2*, 573–581.

30. Lai, F.-J.; Sarma, L. S.; Chou, H.-L.; Liu, D.-G.; Hsieh, C.-A.; Lee, J.-F.; Hwang, B.-J. Architecture of Bimetallic Pt$_x$Co$_{1-x}$ Electrocatalysts for Oxygen Reduction Reaction As Investigated by X-ray Absorption Spectroscopy. *J. Phys. Chem. C* **2009**, *113*, 12674–12681.

31. Dong, W.; Kresse, G.; Hafner, J. Dissociative Adsorption of H$_2$ on the Pd(111) Surface. *J. Mol. Catal. A* **1997**, *119*, 69–76.

32. Chen, C. H.; Hwang, B. J.; Wang, G. R.; Sarma, L. S.; Tang, M. T.; Liu, D. G.; Lee, J. F. Nucleation and Growth Mechanism of Pd/Pt Bimetallic Clusters in Sodium Bis(2-ethylhexyl)sulfosuccinate (AOT) Reverse Micelles as Studied by in Situ X-ray Absorption Spectroscopy. *J. Phys. Chem. B* **2005**, *109*, 21566–21575.

33. Chen, C. H.; Sarma, L. S.; Chen, J. M.; Shih, S. C.; Wang, G. R.; Liu, D. G.; Tang, M. T.; Lee, J. F.; Hwang, B. J. Architecture of Pd–Au Bimetallic Nanoparticles in Sodium Bis(2-ethylhexyl)sulfosuccinate Reverse Micelles As Investigated by X-ray Absorption Spectroscopy. *ACS Nano* **2007**, *1*, 114–125.

34. Chen, C. H.; Sarma, L. S.; Wang, G. R.; Chen, J. M.; Shih, S. C.; Tang, M. T.; Liu, D. G.; Lee, J. F.; Chen, J. M.; Hwang, B. J. Formation of Bimetallic Ag–Pd Nanoclusters *via* the Reaction between Ag Nanoclusters and Pd^{2+} Ions. *J. Phys. Chem. B* **2006**, *110*, 10287–10295.

35. Hwang, B. J.; Chen, C. H.; Sarma, L. S.; Chen, J. M.; Wang, G. R.; Tang, M. T.; Liu, D. G.; Lee, J. F. Probing the Formation Mechanism and Chemical States of Carbon-Supported Pt–Ru Nanoparticles by in Situ X-ray Absorption Spectroscopy. *J. Phys. Chem. B* **2006**, *110*, 6475–6482.

36. Sarma, L. S.; Chen, C. H.; Kumar, S. M. S.; Wang, G. R.; Yen, S. C.; Liu, D. G.; Sheu, H. S.; Yu, K. L.; Tang, M. T.; Lee, J. F. Formation of Pt–Ru Nanoparticles in Ethylene Glycol Solution: An in Situ X-ray Absorption Spectroscopy Study. *Langmuir* **2007**, *23*, 5802–5809.

37. Wang, D. Y.; Chen, C. H.; Yen, H. C.; Lin, Y. L.; Huang, P. Y.; Hwang, B. J.; Chen, C. C. Chemical Transformation from FePt to Fe$_{1-x}$PtM$_x$ (M = Ru, Ni, Sn) Nanocrystals by a Cation Redox Reaction: X-ray Absorption Spectroscopic Studies. *J. Am. Chem. Soc.* **2007**, *129*, 1538–1540.

38. Hwang, B. J.; Tsai, Y. W.; Sarma, L. S.; Tseng, Y. L.; Liu, D. G.; Lee, J. F. Genesis of Bimetallic Pt–Cu Clusters in Reverse Micelles Investigated by in Situ X-ray Absorption Spectroscopy. *J. Phys. Chem. B* **2004**, *108*, 20427–20434.

39. Hwang, B. J.; Sarma, L. S.; Chen, J. M.; Chen, C. H.; Shih, S. C.; Wang, G. R.; Liu, D. G.; Lee, J. F.; Tang, M. T. Structural Models and Atomic Distribution of Bimetallic Nanoparticles as Investigated by X-ray Absorption Spectroscopy. *J. Am. Chem. Soc.* **2005**, *127*, 11140–11145.

40. Papageorgopoulos, D. C.; Keijzer, M.; Veldhuis, J. B. J.; de Bruijn, F. A. CO Tolerance of Pd-Rich Platinum Palladium Carbon-Supported Electrocatalysts. *J. Electrochem. Soc.* **2002**, *149*, A1400–A1404.

41. Green, C. L.; Kucernak, A. Determination of the Platinum and Ruthenium Surface Areas in Platinum–Ruthenium Alloy Electrocatalysts by Underpotential Deposition of Copper. I. Unsupported Catalysts. *J. Phys. Chem. B* **2002**, *106*, 1036–1047.

42. Sarma, L. S.; Taufany, F.; Hwang, B. J. *Electrocatalysis of Direct Methanol Fuel Cells: From Fundamentals to Applications*; Liu, H., Zhang, J., Eds.; Wiley-VCH: Weinheim, 2009; pp 144–145.

43. Hwang, B. J.; Lin, S. H. Reaction Mechanism of Electroless Deposition: Observations of Morphology Evolution during Nucleation and Growth *via* Tapping Mode AFM. *J. Electrochem. Soc.* **1995**, *142*, 3749–3754.

44. Loffreda, D.; Simon, D.; Sautet, P. Dependence of Stretching Frequency on Surface Coverage and Adsorbate-Adsorbate Interactions: a Density-Functional Theory Approach of CO on Pd (111). *Surf. Sci.* **1999**, *425*, 68–80.

45. Honkala, K.; Pirilä, P.; Laasonen, K. CO and NO Adsorption and Co-adsorption on the Pd(1 1 1) Surface. *Surf. Sci.* **2001**, *489*, 72–82.

46. Lim, B.; Wang, J.; Camargo, P. H. C.; Jiang, M.; Kim, M. J.; Xia, Y. Facile Synthesis of Bimetallic Nanoplates Consisting of Pd Cores and Pt Shells through Seeded Epitaxial Growth. *Nano Lett.* **2008**, *8*, 2535–2540.

47. Huang, W. J.; Zuo, J. M.; Jiang, B.; Kwon, K. W.; Shim, M. Sub-Angstrom-Resolution Diffractive Imaging of Single Nanocrystals. *Nat. Phys.* **2009**, *5*, 129–133.

48. Xiong, Y.; Xia, Y. Shape-Controlled Synthesis of Metal Nanostructures: The Case of Palladium. *Adv. Mater.* **2007**, *19*, 3385–3391.

49. Yang, H.; Alonso-Vante, N.; Léger, J. M.; Lamy, C. Tailoring, Structure, and Activity of Carbon-Supported Nanosized Pt–Cr Alloy Electrocatalysts for Oxygen Reduction in Pure and Methanol-Containing Electrolytes. *J. Phys. Chem. B* **2004**, *108*, 1938–1947.

50. Yang, H.; Vogel, W.; Lamy, C.; Alonso-Vante, N. Structure and Electrocatalytic Activity of Carbon-Supported Pt–Ni Alloy Nanoparticles Toward the Oxygen Reduction Reaction. *J. Phys. Chem. B* **2004**, *108*, 11024–11034.

51. The guidelines for data collection modes for EXAFS measurements and user-controlled parameters: http://ixs.iit.edu/subcommittee_reports/sc/sc00report.pdf.

52. The guidelines for errors reporting: http://ixs.iit.edu/subcommittee_reports/sc/err.

53. Vanderbilt, D. Soft Self-Consistent Pseudopotentials in a Generalized Eigenvalue Formalism. *Phys. Rev. B* **1990**, *41*, 7892–7895.

54. Blöchl, P. E. Projector Augmented-Wave Method. *Phys. Rev. B* **1994**, *50*, 17953–17979.

55. Kresse, G.; Joubert, D. From Ultrasoft Pseudopotentials to the Projector Augmented-Wave Method. *Phys. Rev. B* **1999**, *59*, 1758–1775.

56. Hu, P.; King, D. A.; Crampin, S.; Lee, M. H.; Payne, M. C. Gradient Corrections in Density Functional Theory Calculations for Surfaces: Co on Pd{110}. *Chem. Phys. Lett.* **1994**, *230*, 501–506.

57. Perdew, J. P.; Chevary, J. A.; Vosko, S. H.; Jackson, K. A.; Pederson, M. R.; Singh, D. J.; Fiolhais, C. Atoms, Molecules,

Solids, and Surfaces: Applications of the Generalized Gradient Approximation for Exchange and Correlation. *Phys. Rev. B* **1992**, *46*, 6671–6687.

58. Kresse, G.; Hafner, J. Ab Initio Molecular Dynamics for Liquid Metals. *Phys. Rev. B* **1993**, *47*, 558–561.

59. Kresse, G.; Furthmüller, J. Efficient Iterative Schemes for Ab Initio Total-Energy Calculations Using a Plane-Wave Basis Set. *Phys. Rev. B* **1996**, *54*, 11169–11186.

60. Kresse, G.; Furthmüller Efficiency of Ab-Initio Total Energy Calculations for Metals and Semiconductors Using a Plane-Wave Basis Set. *J. Comput. Mater. Sci.* **1996**, *6*, 15.